



Article

The Dynamics and Microphysical Characteristics of the Convection Producing the Record-Breaking Hourly Precipitation on 20 July 2021 in Zhengzhou, China

Kun Zhao ^{1,*},[†], Xin Xu ^{1,†} , Ming Xue ^{1,2} , Zhe-Min Tan ¹, Hao Huang ¹ , Ang Zhou ¹ , Xueqi Fan ¹, Qiqing Liu ¹, Chenli Wang ¹, Juan Fang ¹, Wen-Chau Lee ³, Qinghong Zhang ⁴, Fan Zhang ⁵ , Gang Chen ⁶ and Ji Yang ⁶

- ¹ Key Laboratory of Mesoscale Severe Weather/Ministry of Education, and School of Atmospheric Sciences, Nanjing University, Nanjing 210023, China; zmtan@nju.edu.cn (Z.-M.T.)
- ² Center for Analysis and Prediction of Storms, School of Meteorology, University of Oklahoma, Norman, OK 73072, USA
- ³ Earth Observing Laboratory, National Center for Atmospheric Research, Boulder, CO 80301, USA
- ⁴ Department of Atmospheric and Oceanic Sciences, School of Physics, Peking University, Beijing 100871, China
- ⁵ State Key Laboratory of Severe Weather, Chinese Academy of Meteorological Sciences, Beijing 100081, China
- ⁶ Nanjing Joint Institute for Atmospheric Sciences, Nanjing 210009, China
- * Correspondence: zhaokun@nju.edu.cn
- [†] These authors contributed equally to this work.

Abstract: An hourly rainfall of 201.9 mm fell in Zhengzhou on 20 July 2021, breaking the hourly rainfall record of mainland China and causing severe urban flooding and human casualties. This observation-based study investigates the associated convective-scale and mesoscale dynamics and microphysical processes using disdrometer and polarimetric radar observations aided by retrievals from the Variational Doppler Radar Analysis System. The synoptic flow forcing brought abundant moisture from the oceans and converged at Zhengzhou; then, the extreme rainfall was produced by a slow-moving convective storm that persisted throughout the hour over Zhengzhou. Unusually high concentrations of raindrops of all sizes (showing combined properties of maritime and continental convection) are revealed by the disdrometer data, whereas the polarimetric radar data suggest that both ice-based and warm rain processes were important contributors to the total rainfall. High precipitation efficiency was achieved with an erect updraft at the low levels, whereas enhanced easterly inflows kept the storm moving slowly. The interaction between convective-scale and mesoscale dynamics and microphysical processes within the favorable synoptic conditions led to this extremely heavy rainfall.

Keywords: extreme rainfall; dynamics and microphysics; slow-moving convection



Citation: Zhao, K.; Xu, X.; Xue, M.; Tan, Z.-M.; Huang, H.; Zhou, A.; Fan, X.; Liu, Q.; Wang, C.; Fang, J.; et al. The Dynamics and Microphysical Characteristics of the Convection Producing the Record-Breaking Hourly Precipitation on 20 July 2021 in Zhengzhou, China. *Remote Sens.* **2023**, *15*, 4511. <https://doi.org/10.3390/rs15184511>

Academic Editor: Angelica Tarpanelli

Received: 4 July 2023

Revised: 6 September 2023

Accepted: 7 September 2023

Published: 13 September 2023



Copyright: © 2023 by the authors. Licensee MDPI, Basel, Switzerland. This article is an open access article distributed under the terms and conditions of the Creative Commons Attribution (CC BY) license (<https://creativecommons.org/licenses/by/4.0/>).

1. Introduction

On 20 July 2021, the 24-h rainfall (0000 to 2400 LST) reached 612.9 mm (Figure 1a) in Zhengzhou (ZZ) city, Henan Province, China, approaching the city's average annual rainfall amount of ~640 mm. Between 1600 and 1700 LST, an hourly rainfall rate of 201.9 mm was observed, which broke China's previous record of 198.5 mm h⁻¹ set in 1975 in the same province (known as the "75.8" rainstorm [1]). At least 302 lives were lost in this record-setting extreme rainfall that flooded ZZ, including the city's subway system and underground tunnels.

This extreme rainfall period was part of a week-long (from 17 to 23 July 2021, hereafter named as the "21.7" rainstorm) heavy rainfall episode in a broad region of Henan Province near the foothills of the Taihang and Funiu Mountains. This prolonged extreme heavy rainfall event was accompanied by abnormal synoptic conditions in East Asia (Figure 1b), including (1) the western Pacific subtropical high (WPSH) shifting northward, (2) Typhoon

In-Fa located east of Taiwan, and (3) the 200 hPa South Asian high (SAH) extending northeastward, that produced ingredients conducive to heavy rainfall in Henan [1–8]. A water vapor channel, referred to as an atmospheric river (AR) in other regions [9], was established between Typhoon In-Fa and the WPSH (indicated by the strong water vapor flux in Figure 1b) that transported abundant tropical oceanic moisture over 500 km inland. The extension of the 200 hPa SAH led to upper-level wind divergence in the vicinity of ZZ, also providing favorable upper-level conditions for the development of deep convection in ZZ.

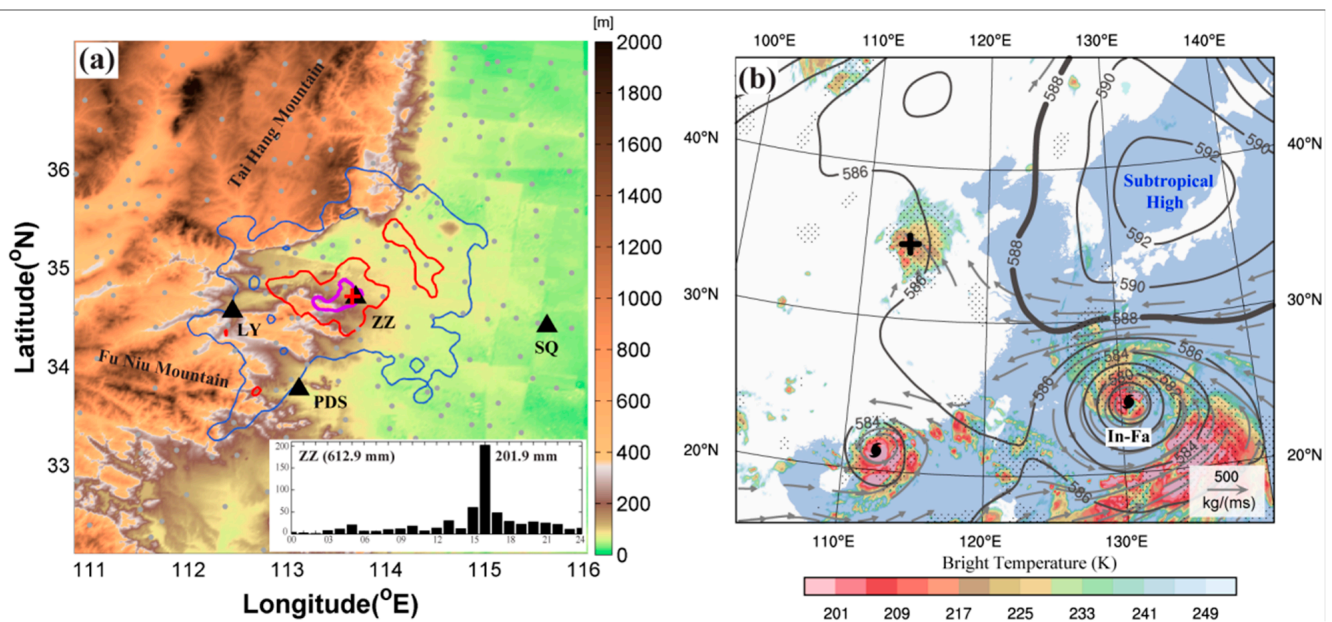


Figure 1. (a) Distribution map of ground instruments on the digital terrain elevation map around ZZ. Triangles denote the locations of four operational radars. Blue, red, and purple contours indicate the 24-h accumulated rainfall over 100, 250, and 400 mm on 20 July, respectively. The time series of the hourly rainfall from the ZZ national surface station (indicated by a red cross) is also shown in the bottom right corner of the figure. (b) Circulation fields at 0800 LST on 20 July 2021. Gray contours represent geopotential height at 500 hPa, and the bold line indicates the location of the western Pacific subtropical high (WPSH). Vectors are vertically integrated water vapor flux (in the layer of 1000–300 hPa) larger than $150 \text{ kg m}^{-1} \text{ s}^{-1}$, and black dots indicate the wind divergence at 200 hPa that is larger than 10^{-5} s^{-1} . Shading represents the $10.8 \mu\text{m}$ infrared brightness temperature from FY-4A. The black cross indicates the location of the ZZ national surface station.

These synoptic conditions that were favorable for the heavy rainfall in Henan Province were identified by the Chinese Meteorological Administration (CMA) in their forecasting operations. Based on operational numerical models and objective forecasting techniques, the National Meteorological Center (NMC) of the CMA predicted an over 250 mm daily rainfall amount in Henan for 20 July one day in advance but failed to predict the extreme intensity and timing of the extreme rainfall in ZZ. The average hourly rainfall (Figure 1a) excluding the period of 1600–1700 LST in ZZ was about 18 mm h^{-1} throughout the day. Heavy rainfall is typically accompanied by single or multiple slow-moving convective storms over an area, whereas the basics involved in the development of flash-flood-producing storms are generally well known [10–12]. The difficulties lie in predicting the exact time, location, and amount of heavy rainfall [13–15]. To generate the extreme rainfall in ZZ, many favorable conditions needed to coexist, and dynamic, thermodynamic, and microphysical processes needed to work in synergy to efficiently convert a large amount of water vapor into precipitation. The “21.7” rainstorm event revealed the ongoing challenges in forecasting the location and amount of extreme hourly rainfall [16,17], even when the environmental conditions are correctly predicted to be very favorable.

Numerical studies were conducted to investigate the possible dynamical mechanism responsible for the production of the “21.7” extreme rainfall [6,18]. The dynamics of this extreme rainfall event were also studied by Sun et al. [19] using the four-dimensional Variational Doppler Radar Analysis System (VDRAS) [20]. Based on the combined observations of the polarimetric radar and disdrometer, the overall variability of microphysical characteristics for the heavy rainfall episode from 19 to 21 July 2021 was examined [21], whereas Yin et al. [22] explored the precipitation efficiency of the “21.7” extreme rainfall using numerical simulation. However, the detailed microphysical processes and their coupling with multiscale dynamical processes to produce the record-breaking hourly rainfall have not yet been investigated. This study focuses on the likely convective and mesoscale dynamics and microphysical processes that transformed the abundant oceanic moisture in the ZZ area to generate this record-breaking hourly rainfall between 1600 and 1700 LST on 20 July 2021. The three-dimensional wind and thermodynamic fields are obtained from the VDRAS, and the corresponding microphysical processes are deduced from the Luoyang (LY) operational polarimetric radar and a disdrometer at the ZZ national surface station.

2. Datasets and Methods

2.1. Datasets

This study used data from the operational observational network operated by the CMA, including 4 operational S-band Doppler radars (ZZ, LY, PDS, and SQ in Figure 1), 19 lightning detection sensors, 6900 automatic weather stations (AWSs), and a second-generation OTT particle size and velocity (PARSIVEL) disdrometer (OTT-2) located at ZZ. These radars perform volume scans at nine elevations (0.5° , 1.5° , 2.4° , 3.4° , 4.3° , 6.0° , 9.9° , 14.6° , and 19.5°) every 6 min, with an unambiguous range (velocity) of 150 km (26.5 m s^{-1}). The LY and ZZ radars can measure polarimetric variables including the differential reflectivity (Z_{DR}), differential propagation phase shift (Φ_{DP}), and specific differential phase (K_{DP}). The disdrometer can measure the number, concentration, and fall speed of raindrops within 32 bins ranging from 0 to 25 mm every minute.

2.2. Methods

The procedure for the data quality control of the OTT-2 data was introduced in Chen et al. [23]. The calculation of the raindrop size distribution (DSD), including the generalized intercept parameter (N_w) and mass-weighted mean diameter (D_m) followed Bringi et al. [24]. The radar data were firstly quality controlled to remove the ground clutter and velocity alias and correct the effect of partial beam blockage and the Z_{DR} bias [25], then bilinearly interpolated onto constant-altitude planes with a 1 km grid spacing in both the horizontal and vertical directions [26]. The ten hydrometeor types (drizzle (DZ), rain (RA), big drops (BD), ice crystals (IC), vertical aligned ice (VI), aggregates (AG), wet snow (WS), high-density graupel (HG), low-density graupel (LG), and hail (HA)) were identified from polarimetric radar data based on the fuzzy logic method presented in Dolan et al. [27], and the retrieval of ice water content (IWC) and liquid water content (LWC) mainly involved a method similar to that in Cifelli et al. [28] but with the LWCs for non-solid hydrometeors calculated from the K_{DP} . The LWC- K_{DP} relationship was fitted through the DSD data using the T-matrix method [29]. The precipitation efficiency was calculated using the rain rate divided by the total water vapor within a layer from 3 to 5 km heights [30].

The VDRAS is a four-dimensional variational data assimilation system that assimilates radar observations (i.e., radar reflectivity and radial velocity) and surface observations with the background provided by the weather research and forecasting (WRF) model [20,31]. In the VDRAS analysis, radar observations from ZZ, SQ, PDS, and LY (Figure 1) with a 6-min interval, together with surface observations of temperature and wind from the 6900 AWSs with a 5-min interval were assimilated. The VDRAS domain was centered at the ZZ radar with a horizontal resolution of 3 km and 0.4 km vertical spacing from 0900 to 2000 on 20 July 2021.

3. Results

3.1. Mesoscale and Convective Dynamical Processes

Widespread precipitation occurred in the central and northern parts of the Henan Province, with convective activities mostly in the mountainous areas west of ZZ on 20 July 2021. Figure 2a shows the horizontal winds at 0.6 km above the mean sea level (MSL) obtained from the VADRS analysis at 1200 LST, i.e., four hours before the extreme hourly rainfall in ZZ. Predominantly easterlies from the east of Henan were blocked on the southeastern slope of the Taihang Mountains and turned into northeasterlies in the form of a barrier jet [32] (see Supplementary Figure S1) that funneled into the valley towards LY, whereas east of the Funiu Mountains was southerly flows towards the Song Mountains (SM) and ZZ. Together with the easterly flows east of ZZ, a three-way low-level convergence was set up at ZZ that had the potential to produce extreme rainfall. In the lower troposphere (Figure 2b), there was a mesoscale vortex located west of ZZ [18,33]. The horizontal winds of this low-level mesovortex were primarily southerlies/southwesterlies over ZZ, which showed an increasing trend from 1000 LST, with a moderate speed of $\sim 14 \text{ m s}^{-1}$ at 1600 LST (see Supplement Figure S2). By 1600 LST, the low-level convergence at ZZ was strengthened, with the maximum more than doubled from $1.4 \times 10^{-3} \text{ s}^{-1}$ at 1200 to $3.5 \times 10^{-3} \text{ s}^{-1}$ (Figure 2c). Easterly winds increased toward ZZ, leading to the enhancement of convergence.

A sounding extracted from the 1200 LST VDRAS analysis 150 km southeast of ZZ (Figure 2e) exhibited a well-mixed boundary layer due to solar insolation, with a low lifting condensation level (LCL) of 685 m MSL and a moderate convective available potential energy (CAPE) of 2670 J kg^{-1} . The net low-level moisture convergence into a budget box over ZZ (red box in Figure 2a) steadily increased from 1100 LST, reaching a maximum at 1600 LST and quadrupling over the period. Most of the increase was due to the increase in inward flux through the eastern boundary and the decrease in outward flux through the western boundary (Figure 2d). The large positive flux through the southern boundary also increased somewhat, whereas the northern boundary flux remained negative but small. Because of the continuous moistening, the low-level inflow was near saturation (Figure 2e), tending to suppress the evaporative cooling of rainfall. In consequence, the storm produced a relatively weak cold pool of about 2 K, whose leading edge was near ZZ (Figure 2f).

Tracing back in time, the convective storm (labeled CS in Figure 3) that reached ZZ by 1600 LST (Figure 3c) was initiated before 1200 LST along the southern slope of the SM, $\sim 55 \text{ km}$ southwest of ZZ (Figure 3a). This storm was characterized by a maximum reflectivity of $\sim 55 \text{ dBZ}$, with the 30 dBZ echo reaching $\sim 6.5 \text{ km}$ altitude and a few lightning flashes. The storm moved northeastward at a speed of $\sim 5 \text{ m s}^{-1}$ and reached the western edge of ZZ at around 1500 LST (Figure 3b). Because of the three-way low-level convergence over ZZ, the storm became quasi-stationary between 1600 LST and 1700 LST, producing the extreme hourly precipitation. In the west–east direction, the cold pool density current was balanced by the low-level easterly inflow, which were 6.2 m s^{-1} and -6.4 m s^{-1} , respectively, between 1600 and 1700 LST (Figure 2g). In the south–north direction, the low-level southerly and northerly winds were also nearly in balance, with mean values of 4.8 and -4.0 m s^{-1} , respectively (Figure 2h). The above balances between multiscale flows are in agreement with the numerical results of Wei et al. [18] and contributed to the quasi-stationarity of the convective storm in ZZ. The slow-moving storm reached its peak intensity (Figure 3c,d) with increased lightning. The maximum 30 dBZ echo height reached 12 km in the east–west vertical cross section through the precipitation center of the storm (Figure 3e), indicating enhanced convection intensity [34,35]. This deep, erect convection favored higher precipitation efficiency [36,37]. The VDRAS analysis showed that at 1600 LST, the low-level easterly inflows entered the storm updraft below 3 km and the air and ice aggregates exited the front (i.e., east side) of the storm above a 5 km altitude (Figure 3f). These falling ice aggregates could have helped maintain the storm by destabilizing the storm inflow [38].

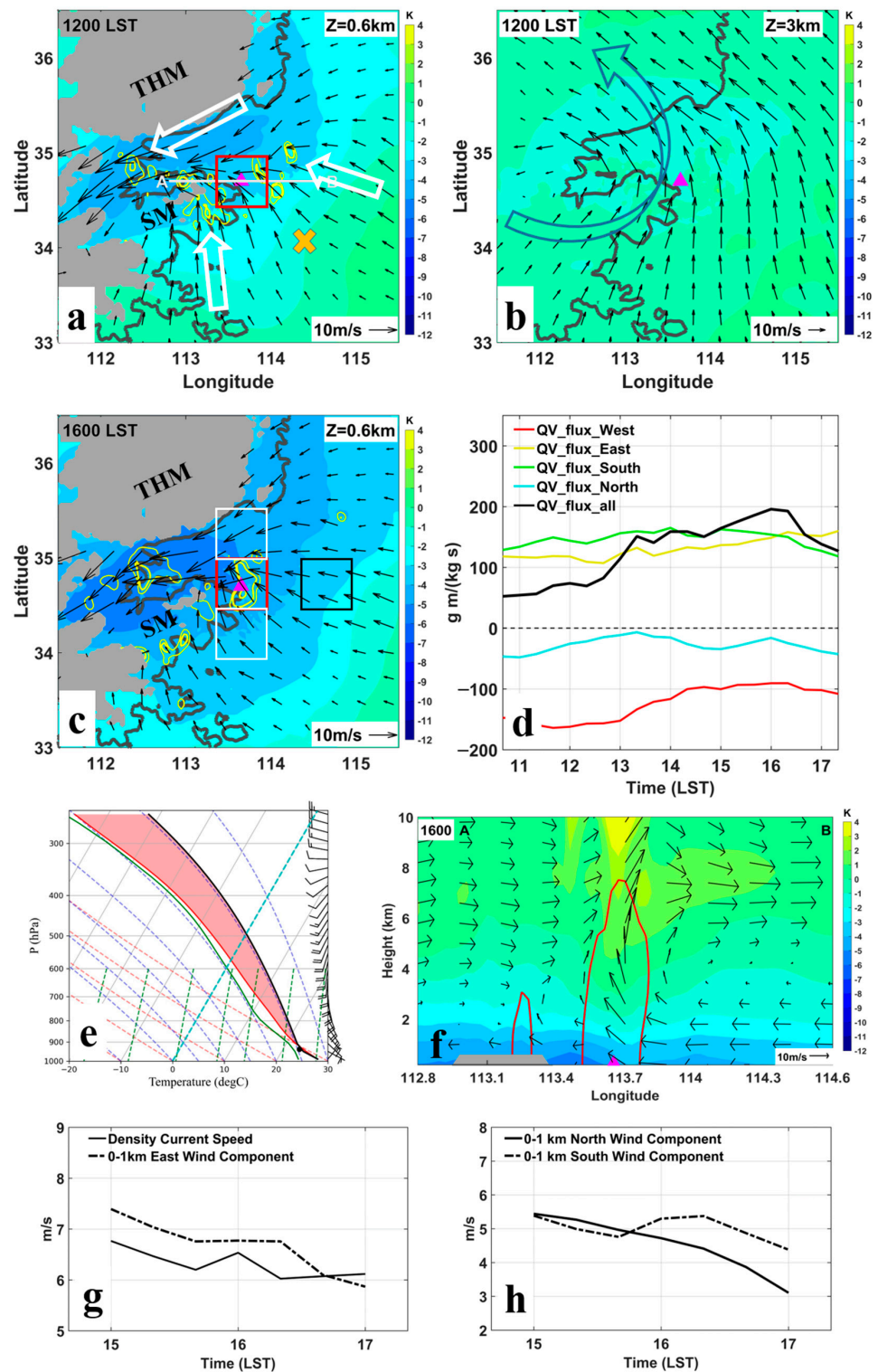


Figure 2. (a) Perturbation temperature (shading) and horizontal wind vectors at 0.6 km MSL in the VDRAS analysis at 1200 LST on 20 July 2021. Yellow contours are the horizontal convergence starting from $-1 \times 10^{-3} \text{ s}^{-1}$ at an interval of $-2 \times 10^{-3} \text{ s}^{-1}$. Black lines are 600 m terrain elevation contours and the purple triangle indicates the location of the record-breaking hourly precipitation rain gauge station in ZZ. (b) As (a) but at 3 km. The curved arrow represents the mesoscale vortex. (c) As (a) but at 1600 LST. (d) 0–3 km moisture fluxes through the 4 borders of a 60×60 km box region covering the ZZ city (red box in (a,c)) and net flux into the box (positive into the box), based on the VADRS analysis. (e) Inflow environment sounding located at 150 km southeast of ZZ (yellow X in (a)) extracted from

the VDRAS analysis at 1200 LST with the red, green, and black solid lines representing the temperature profile, dew point profile, and the parcel ascent curve, respectively. (f) Perturbation temperature (shading) and wind vectors in the west–east vertical cross section through the center of ZZ city (line AB in (c)) in VADRAS analysis at 1600 LST. Red contours denote 40 dBZ radar reflectivity. (g) Evolution of cold pool density current and low-level easterlies between 0 and 1 km calculated within the red and black boxes in (c). (h) Evolution of the southerly and northerly wind components to the south and north of the storm (see the white boxes in (c)) over ZZ, respectively.

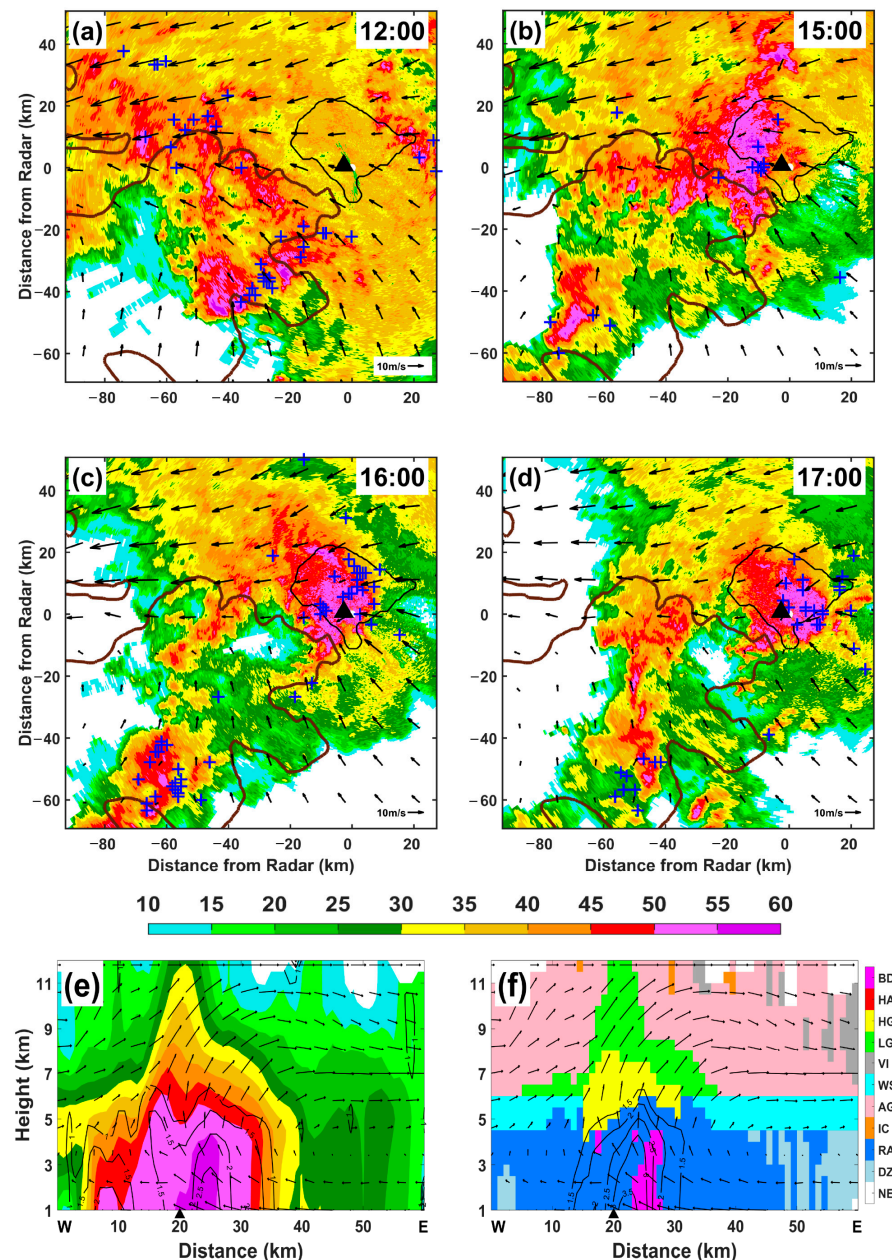


Figure 3. Observed radar reflectivity (color shading; units: dBZ) and horizontal winds at 600 m MSL at (a) 1200 LST, (b) 1500 LST, (c) 1600 LST, and (d) 1700 LST on 20 July 2021. A terrain height of 200 m is indicated by the bold brown contours. The black line represents the urban area of ZZ, and the triangle indicates the national surface station with the hourly extreme rainfall in ZZ. The blue pluses indicate that the lightning occurred 30 min before and after the radar time. SM indicates the Song Mountain. West–east cross sections of (e) Z_H (color shading) and Z_{DR} (contours) and (f) hydrometeor types based on hydrometeor classification algorithm (shading) and K_{DP} (contours) across the rainfall center at 1600 LST.

3.2. Microphysical Processes in the Extreme Rainfall

3.2.1. Vertical Distributions of Hydrometeors

The hydrometeor classification algorithm (HCA [27]) based on the polarimetric radar data indicates graupels (large rain drops) above (below) the freezing level (Figure 3f). The combination of the large reflectivity Z_H (~ 58 dBZ), differential reflectivity Z_{DR} (~ 3.0 dB), and differential phase K_{DP} ($\sim 4^\circ \text{ km}^{-1}$) near the surface beneath the updraft signals intense rainfall with the presence of large and oblate raindrops [39,40]. Positive Z_{DR} and K_{DP} columns were collocated with the updraft, where the region of $Z_{DR} > 1.0$ dB and $K_{DP} > 1.5^\circ \text{ km}^{-1}$ extended to a 6.5 km altitude, indicating supercooled liquid particles lifted above the freezing level (~ 5 km) by the strong updrafts (Figure 3e,f) [41,42]. The existence of the supercooled liquid water favored the riming process and the presence of graupel in the updraft region above the freezing level.

The time series of the Z_H , Z_{DR} , and K_{DP} fractions in specified value bins from 1200 to 2000 LST on 20 July 2021 are presented in Figure 4a–c. The polarimetric radar variables come from the 30×30 km box centered at the CS (labeled in Figure 3) at 2.0 km MSL. As the CS developed to the mature stage between 1600 and 1700 LST, the radar reflectivity values were frequently above 50 dBZ. About 20% of the Z_{DR} samples exceeded 2.0 dB in this hour, which was obviously higher than in any other hour, indicating abundant large raindrops formed in the CS. In addition, the fractions with a high K_{DP} value (over $3.0^\circ \text{ km}^{-1}$) also peaked in the same hour, suggesting the dominance of extreme liquid water contents and instant rain rates at this vertical level. The significantly higher fractions of large polarimetric radar variables compared with other hours are consistent with the hourly extreme rainfall at the surface.

The vertical structure of the polarimetric radar variables in the region of radar-observed extreme rainfall near ZZ (K_{DP} higher than 4° km^{-1} , approximately 160 mm h^{-1} based on the radar-estimated rainfall) is illustrated in Figure 4d. More than 95% of the extreme rainfall occurred in the strong updraft region, as shown in Figure 3f. Between 12 and 8 km, Z_H increased rapidly, whereas Z_{DR} decreased slightly with decreasing height; the Z_{DR} was around 0 dB, suggesting there was aggregation in this layer [43]. Between 8 km and 5 km (the 0° C level), the increase in both Z_H and K_{DP} indicates the existence of more supercooled liquid drops [41]. The increase in Z_H , Z_{DR} , and K_{DP} towards the 0° C level reflects the occurrence of active riming processes, as further confirmed by the normalized frequency of hydrometeors showing that large ice particles (graupel or hail) dominate in this layer (Figure 4e). Below the 0° C level, Z_H , Z_{DR} , and K_{DP} continuously increased toward the ground, indicating active warm rain processes of coalescence and accretion [44,45] that help increase the raindrop sizes and enhance precipitation. The enhanced Z_H and Z_{DR} within 1 km below the 0° C level can be partly attributed to the melting of graupel and hail because of the increase in the dielectric constant and aspect ratio [46,47].

The radar-derived IWC and LWC analysis shows a rapid increase in LWC below the melting level, mainly through the accretion of cloud drops along with the auto-conversion process. The maximum LWC is about 6.2 g m^{-3} near the ground, less than twice the IWC maximum (about 3.9 g m^{-3}), suggesting that both ice and warm rain processes have important contributions to the surface extreme rainfall. This can be explained by the interactions between the kinematic and microphysical structures of the convective storm under favorable environmental conditions. A low LCL, strong low-level moisture convergence, and a deep warm cloud layer can promote the rapid and efficient conversion of inflow water vapor to cloud drops and then raindrops in the updraft through active warm rain processes [10]. Meanwhile, the strong updraft also transports water vapor and liquid water above the freezing level to promote the production of graupels and hails. Previous studies showed that upright convection has a higher precipitation efficiency than tilted convection because it allows for a more effective collection of cloud condensate by precipitation [36,48]. In this event, because the convective storm was erect, the large raindrops from melting graupels or hailstones can fall through the updraft and grow by accretion and coalescence below the melting layer and contribute to the extreme rainfall.

This suggests an optimal coupling between ice-based and warm rain processes contributed to the extreme hourly rainfall in ZZ.

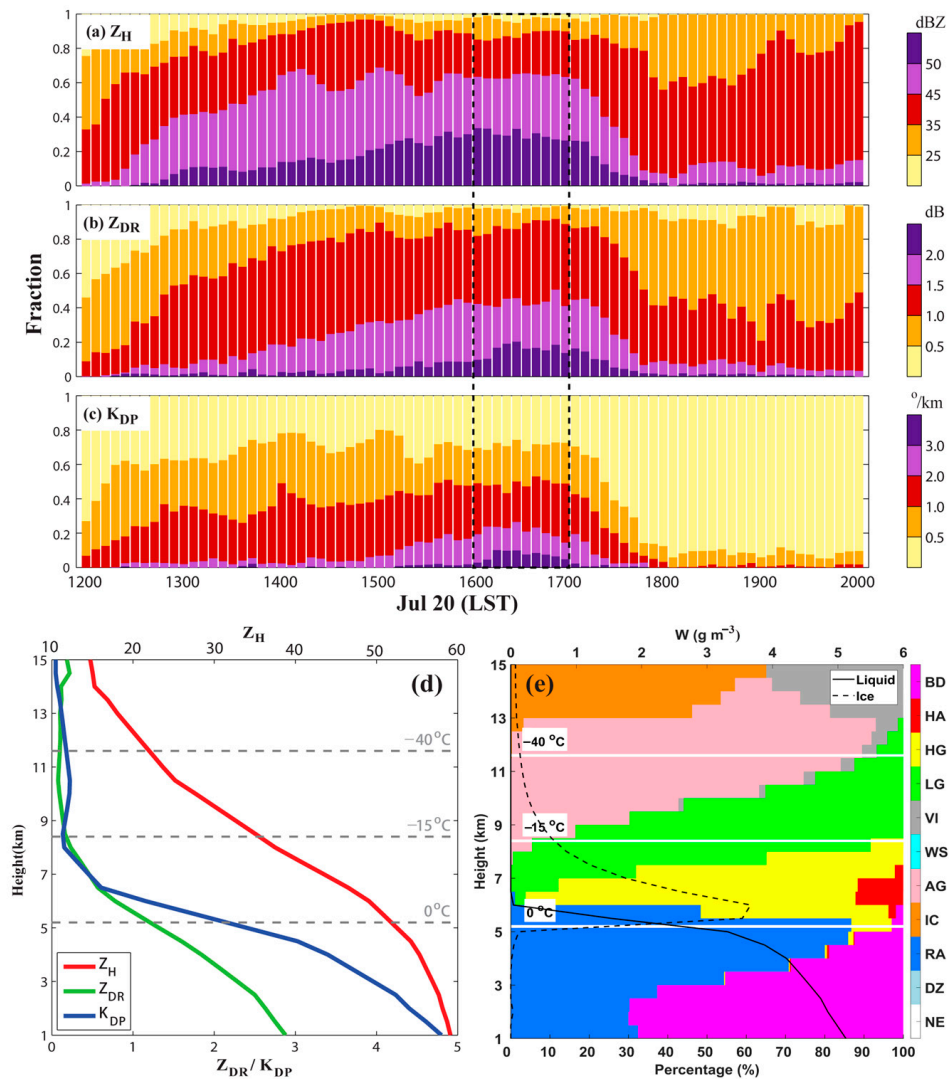


Figure 4. Time series of (a) Z_H , (b) Z_{DR} , and (c) K_{DP} fractions in specified bins at 2.0 km MSL in the 30×30 km box centered on the CS (labeled in Figure 3) from 1200 to 2000 LST. Average profiles of (d) polarimetric radar variables and (e) hydrometeor types (shading), LWC (black solid), and IWC (red dashed) for K_{DP} values higher than $4^{\circ} \text{ km}^{-1}$ near the ZZ national surface station between 1600 and 1700 LST. The label for IWC/LWC is shown at the top of the panel.

3.2.2. The Raindrop Size Distribution on the Ground

The DSD is an important feature of precipitation microphysics [49]. The time series of DSD from 1 min OTT–2 observations at ZZ (Figure 5a) shows that both the drop number and maximum drop diameter increased dramatically between 1600 and 1700 LST. Note that the variations in the DSD during this period represent different parts of the convective storm moving across ZZ. The concentration of small raindrops ($D < 1$ mm) reached as high as $10^4 \text{ m}^{-3} \text{ mm}^{-1}$, with the largest drop diameter being about 7 mm. With the increase in drop concentrations for all particle sizes, the hourly rain rate reached an extreme value of 201.9 mm h^{-1} . The largest contribution (66%) to total rainfall was from mid-size drops (1–3 mm), whereas large drops ($D > 3$ mm) were the second largest contributor (22%). On the other hand, small drops dominated the total number concentration (81.5%) but had the least contribution (12%) to the total rainfall. This is consistent with the large Z_{DR} and high K_{DP} near the surface (Figure 4a).

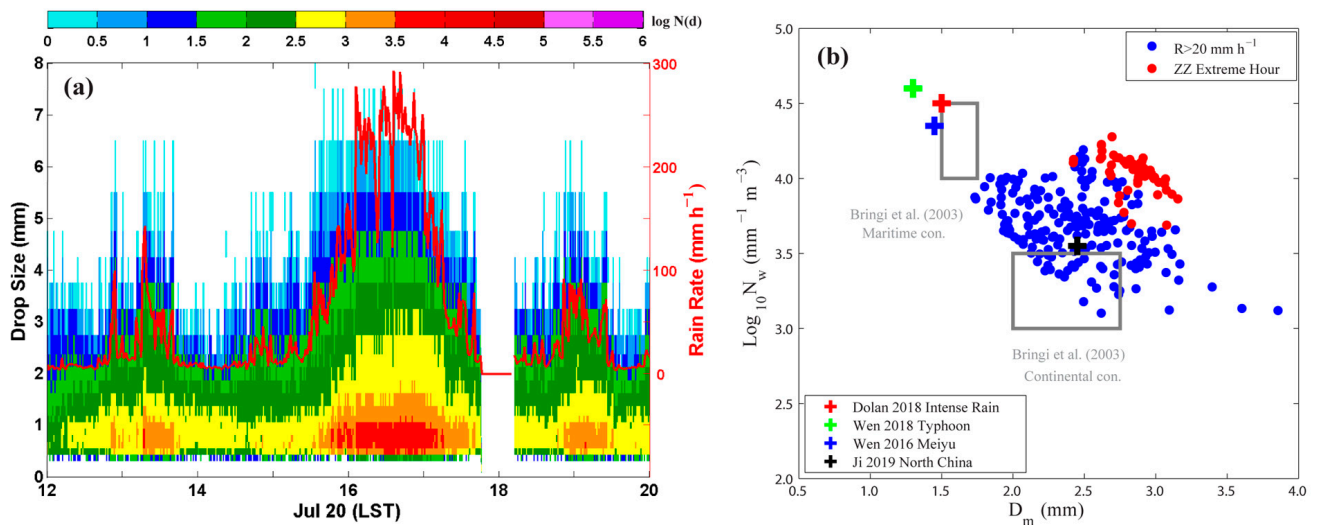


Figure 5. (a) Time series of 1 min DSDs from the OTT disdrometer at the ZZ national surface station. Color shading represents the DSD in logarithmic units of $\text{mm}^{-1} \text{m}^{-3}$ and the y -axis indicates the equivalent volume diameter (mm) of raindrops; the instant rain rate is plotted as the red line. (b) Scatters of N_w (D_m) from the ZZ extreme hourly rainfall between 1600 and 1700 LST (red) and DSD samples with an instant rain rate over 20 mm h^{-1} from 1200 to 2000 LST (blue), respectively. The two gray rectangles represent the maritime and continental convective clusters reported by [24]. The blue, green, black, and red crosses represent the mean values of convective rain in different regions from previous studies [50–53].

The scatter plot of $\log_{10}N_w$ (the generalized intercept parameter, indicating the raindrop concentration) and D_m (mass-weighted mean diameter) in Figure 5b illustrates the unique microphysical characteristics that distinguished the extreme hourly rainfall in ZZ (red dots) from other documented heavy rainfall events produced by typical continental or maritime convection [50–53] as well as other rainfall hours of the “21.7” rainstorm surrounding the extreme rainfall hour (blue dots). The two rectangle boxes in Figure 5b represent the characteristics of maritime and continental convection [24], dominated by warm-rain collision–coalescence processes (higher concentration of small drops) and ice-based microphysical processes (the presence of larger drops from the melting of graupel and hail), respectively [50]. Recent statistical studies have revealed that convective rainfall in South China possesses a maritime nature due to the impact of the East Asian summer monsoons or tropical cyclones [23,52,53], whereas convective rainfall in North China possesses more a continental nature being influenced by the northeast cold vortex and other mid-latitude systems [51,54]. The intense convective rainfall samples (defined as a rain rate $>20 \text{ mm h}^{-1}$ but excluding the period from 1600 to 1700 LST, i.e., blue dots in Figure 5b) show a large variation of D_m and $\log_{10}N_w$ (positioned in between these two boxes), reflecting the presence of ice processes in the ZZ rainfall. During the extreme hourly rainfall in ZZ, the concentrations of both large and small drops increased (Figure 5a), exhibiting the combined properties of maritime (high N_w) and continental (large D_m) convection. This unique characteristic of DSD indicates that both ice-based and warm-rain processes were active in producing the extreme hourly rainfall in ZZ, which is consistent with the microphysical processes inferred from the polarimetric radar observations in the previous subsection. They appear to be the results of extremely rich moisture (like the data of marine precipitation) and sufficiently large CAPE and low-level convergence forcing (that promote deep convection).

4. Conclusions

The “21.7” extreme rainfall event hit Zhengzhou, China on 20 July 2021, causing hundreds of fatalities and great economic losses. In particular, the 1 h precipitation at a

national surface station in ZZ was 201.9 mm between 1600 and 1700 LST, breaking the record for hourly precipitation in mainland China. Our analyses show that the record-breaking hourly precipitation was produced by a quasi-stationary, well-organized, deep convective storm in ZZ that was fed by abundant tropical moisture via an atmospheric river between the WPSH and Typhoon In-Fa. The Taihang Mountains northwest of ZZ played a vital role in turning the environmental low-level easterlies into mountain-parallel northeasterly flows in the north, helping to block the southerly flows from the south into ZZ. The storm that moved into ZZ to produce the extreme hourly rainfall was initiated on the southern slopes of the Song Mountains southwest of ZZ.

The low-level easterly flow into ZZ was steadily enhanced in the hours preceding the extreme rainfall, whereas the airflow out of the ZZ region on its west side weakened in the same period. The flow changes led to a net moisture flux into ZZ that quadrupled in 5 h preceding the extreme hourly rainfall in ZZ. The enhanced low-level easterly flow roughly balanced the relatively weak cold pool density current and kept the storm stationary over ZZ. The rainstorm contained unusually high concentrations of small raindrops with the presence of some very large drops (about 7 mm). The rain DSDs and the polarimetric-radar-derived microphysical properties provided the first observational evidence that both oceanic (high number of raindrops, active warm rain processes) and continental (large raindrops, active ice processes) rain characteristics were active and very efficient in converting the abundant tropical moisture into the record-breaking hourly rainfall. These key dynamical and microphysical processes are summarized schematically in Figure 6.

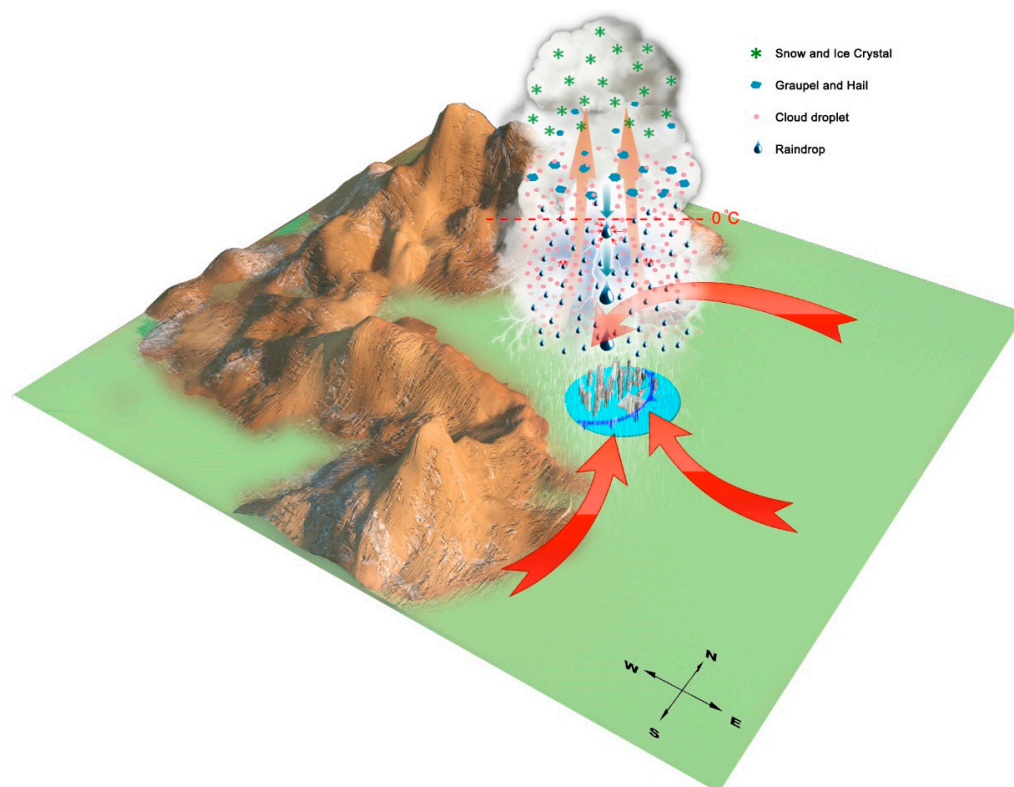


Figure 6. The conceptual model of the maintenance and precipitation microphysics of the convective storm resulting in extreme hourly rainfall in ZZ. The blue line with triangles indicates the cold pool gust front. The red arrows represent the prevalent winds.

This study provides insights into how local extreme rainfall may be better predicted by including mesoscale and convective scale processes together with the well-forecasted favorable synoptic conditions for heavy rainfall. This study also points out the unique DSD differentiating this extreme rainfall event from most other documented precipitation events in different regions of the world. We admit that an MCS should consist of both

convective core and anvil cloud regions, with the latter also likely to contribute to the production of extreme rainfall. In this study, our main purpose was to investigate the key factors causing the record-breaking hourly rainfall in a local ZZ region weather station. According to radar observations, this hourly extreme rainfall was directly caused by the convective cell over ZZ. More observational and modeling studies will be conducted to investigate whether there are optimal and synergetic combinations between dynamics and microphysics in producing the unique DSD identified in the “21.7” extreme rainfall event. To be able to accurately represent within numerical weather prediction models the unique microphysical characteristics of this event and all other important ingredients that act in synergy to produce such record-breaking extreme rainfall and to provide quantitatively accurate operational forecasting with sufficient lead time remain challenging. Gaining insights and understanding of the physical processes and mechanisms involved is critical and this study represents one of the first efforts toward this goal.

Supplementary Materials: The following supporting information can be downloaded at: <https://www.mdpi.com/article/10.3390/rs15184511/s1>, Figure S1: (Top) Terrain elevation (shading) and VDRAS analysis horizontal winds at 0.6 km MSL (vector) at 1200 LST on 20 July 2021. (Bottom) Potential temperature (shading) and VDRAS analysis wind field in the vertical plane along line AB at 1200 LST on 20 July 2021. Red contours indicate the speed of horizontal wind normal to the vertical plane (i.e., nearly parallel to the Taihang Mountain); Figure S2: (Top) Horizontal wind vectors and speed (shading) at 3 km MSL in the VDRAS analysis from 1000 to 1600 LST on 20 July 2021. (Bottom) Time evolution of the mean horizontal wind speed over ZZ at different heights. Reference [55] is cited in Supplementary Materials.

Author Contributions: Conceptualization, K.Z.; Methodology, X.X. and G.C.; Software, H.H., X.F., Q.L. and J.Y.; Formal analysis, A.Z., Q.Z. and F.Z.; Data curation, C.W.; Writing—review & editing, M.X., Z.-M.T., J.F. and W.-C.L. All authors have read and agreed to the published version of the manuscript.

Funding: This work was primarily supported by the National Natural Science Foundation of China (grants 42025501, 4212200198, 41875053, 61827901, and 42122036), the Open Grants of the State Key Laboratory of Severe Weather (2023LASW-A01), the National Key Research and Development Program of China (Grant 2017YFC1501601, 2018YFC1506404).

Data Availability Statement: All freely available data are mentioned in the section on Data and Methods.

Conflicts of Interest: The authors declare no conflict of interest.

References

1. Ding, Y. On the study of the unprecedented heavy rainfall in Henan Province during 4–8 August 1975: Review and assessment. *Acta Meteorol. Sin.* **2015**, *73*, 411–424.
2. Shi, W.; Li, X.; Zeng, M.; Zhang, B.; Wang, H.; Zhu, K.; Zhuge, X. Multi-model comparison and high-resolution regional model forecast analysis for the “7·20” Zhengzhou severe heavy rain. *Trans. Atmos. Sci.* **2021**, *44*, 688–702. [[CrossRef](#)]
3. Sun, W.; Yu, R.; Li, J.; Yuan, W. Three-Dimensional Circulation Structure of Summer Heavy Rainfall in Central North China. *Weather Forecast.* **2015**, *30*, 238–250. [[CrossRef](#)]
4. Tao, S. *Rainstorms in China*; Science Press: Beijing, China, 1980.
5. Wu, G. *Dynamics of the Formation and Variation of Subtropical Anticyclones*; Science Press: Beijing, China, 2002.
6. Yin, J.; Gu, H.; Liang, X.; Yu, M.; Sun, J.; Xie, Y.; Li, F.; Wu, C. A Possible Dynamic Mechanism for Rapid Production of the Extreme Hourly Rainfall in Zhengzhou City on 20 July 2021. *J. Meteorol. Res.* **2021**, *36*, 6–25. [[CrossRef](#)]
7. Zhang, D.-L.; Lin, Y.; Zhao, P.; Yu, X.; Wang, S.; Kang, H.; Ding, Y. The Beijing extreme rainfall of 21 July 2012: “Right results” but for wrong reasons. *Geophys. Res. Lett.* **2013**, *40*, 1426–1431. [[CrossRef](#)]
8. Zhang, X.; Yang, H.; Wang, X.; Shen, L.; Wang, d.; Li, H. Analysis on characteristic and abnormality of atmospheric circulations of the July 2021 extreme precipitation in Henan. *Trans. Atmos. Sci.* **2021**, *44*, 672–687.
9. Ralph, F.M.; Dettinger, M.D.; Cairns, M.M.; Galarneau, T.J.; Eylander, J. Defining “Atmospheric River”: How the Glossary of Meteorology Helped Resolve a Debate. *Bull. Am. Meteorol. Soc.* **2018**, *99*, 837–839. [[CrossRef](#)]
10. Doswell, C.A.; Brooks, H.E.; Maddox, R.A. Flash Flood Forecasting: An Ingredients-Based Method-ology. *Weather Forecast.* **1996**, *11*, 560–581. [[CrossRef](#)]
11. Konrad, C.E. Synoptic-Scale Features Associated with Warm Season Heavy Rainfall over the Interior Southeastern United States. *Weather Forecast.* **1997**, *12*, 557–571. [[CrossRef](#)]

12. Luo, Y.; Wu, M.; Ren, F.; Li, J.; Wong, W.-K. Synoptic Situations of Extreme Hourly Precipitation over China. *J. Clim.* **2016**, *29*, 8703–8719. [[CrossRef](#)]
13. Ding, Y. The major advances and development process of the theory of heavy rainfalls in China. *Torrential Rain Disasters* **2019**, *38*, 395–406.
14. Li, Z.; Chen, Y.; Zhang, X.; Wang, Y.; Dai, K.; Zhang, L. Development and thinking of torrential rain forecasting operation in National Meteorological Center. *Torrential Rain Disasters* **2019**, *38*, 407–415. [[CrossRef](#)]
15. Schumacher, R.S. *Heavy Rainfall and Flash Flooding*; Oxford University Press: Oxford, UK, 2017. [[CrossRef](#)]
16. Zhang, Y.; Yu, H.; Zhang, M.; Yang, Y.; Meng, Z. Uncertainties and error growth in forecasting the record-breaking rainfall in Zhengzhou, Henan on 19–20 July 2021. *Sci. China Earth Sci.* **2022**, *65*, 1903–1920. [[CrossRef](#)]
17. Zhu, K.F.; Zhang, C.; Xue, M.; Yang, N. Predictability and skill of convection-permitting ensemble forecast systems in predicting the record-breaking “21.7” extreme rainfall event in Henan Province, China. *Sci. China Earth Sci.* **2022**, *65*, 1879–1902. [[CrossRef](#)]
18. Wei, P.; Xu, X.; Xue, M.; Zhang, C.; Wang, Y.; Zhao, K.; Zhou, A.; Zhang, S.; Zhu, K. On the Key Dynamical Processes Supporting the 21.7 Zhengzhou Record-breaking Hourly Rainfall in China. *Adv. Atmos. Sci.* **2023**, *40*, 337–349. [[CrossRef](#)]
19. Sun, J.; Li, R.; Zhang, Q.; Trier, S.B.; Ying, Z.; Xu, J. Mesoscale Factors Contributing to the Extreme Rainstorm on 20 July 2021 in Zhengzhou, China, as Revealed by Rapid Update 4DVar Analysis. *Mon. Weather Rev.* **2023**, *151*, 2153–2176. [[CrossRef](#)]
20. Sun, J.; Crook, N.A. Real-Time Low-Level Wind and Temperature Analysis Using Single WSR-88D Data. *Weather Forecast.* **2001**, *16*, 117–132. [[CrossRef](#)]
21. Chen, G.; Zhao, K.; Lu, Y.; Zheng, Y.; Xue, M.; Tan, Z.; Xu, X.; Huang, H.; Chen, H.; Xu, F.; et al. Variability of microphysical characteristics in the “21.7” Henan extremely heavy rainfall event. *Sci. China Earth Sci.* **2022**, *65*, 1861–1878. [[CrossRef](#)]
22. Yin, L.; Ping, F.; Mao, J.; Jin, S. Analysis on Precipitation Efficiency of the “21.7” Henan Extremely Heavy Rainfall Event. *Adv. Atmos. Sci.* **2023**, *40*, 374–392. [[CrossRef](#)]
23. Chen, G.; Zhao, K.; Wen, L.; Wang, M.; Huang, H.; Wang, M.; Yang, Z.; Zhang, G.; Zhang, P.; Lee, W.-C. Microphysical Characteristics of Three Convective Events with Intense Rainfall Observed by Polarimetric Radar and Disdrometer in Eastern China. *Remote Sens.* **2019**, *11*, 2004. [[CrossRef](#)]
24. Bringi, V.N.; Chandrasekar, V.; Hubbert, J.; Gorgucci, E.; Randeu, W.L.; Schoenhuber, M. Raindrop Size Distribution in Different Climatic Regimes from Disdrometer and Dual-Polarized Radar Analysis. *J. Atmos. Sci.* **2003**, *60*, 354–365. [[CrossRef](#)]
25. Shakti, P.C.; Maki, M.; Shimizu, S.; Maesaka, T.; Kim, D.-S.; Lee, D.-I.; Iida, H. Correction of Reflectivity in the Presence of Partial Beam Blockage over a Mountainous Region Using X-Band Dual Polarization Radar. *J. Hydrometeorol.* **2013**, *14*, 744–764. [[CrossRef](#)]
26. Mohr, C.G.; Vaughan, R.L. An Economical Procedure for Cartesian Interpolation and Display of Reflectivity Factor Data in Three-Dimensional Space. *J. Appl. Meteorol.* **1979**, *18*, 661–670. [[CrossRef](#)]
27. Dolan, B.; Rutledge, S.A.; Lim, S.; Chandrasekar, V.; Thurai, M. A Robust C-Band Hydrometeor Identification Algorithm and Application to a Long-Term Polarimetric Radar Dataset. *J. Appl. Meteorol. Clim.* **2013**, *52*, 2162–2186. [[CrossRef](#)]
28. Cifelli, R.; Petersen, W.A.; Carey, L.D.; Rutledge, S.A.; Dias, M.A.F.d.S. Radar observations of the kinematic, microphysical, and precipitation characteristics of two MCSs in TRMM LBA. *J. Geophys. Res. Atmos.* **2002**, *107*, LBA 44-1–LBA 44-16. [[CrossRef](#)]
29. Mishchenko, M.I.; Travis, L.D.; Mackowski, D.W. T-matrix computations of light scattering by nonspherical particles: A review. *J. Quant. Spectrosc. Radiat. Transf.* **1996**, *55*, 535–575. [[CrossRef](#)]
30. Wang, M.; Zhao, K.; Xue, M.; Zhang, G.; Liu, S.; Wen, L.; Chen, G. Precipitation microphysics characteristics of a Typhoon Matmo (2014) rainband after landfall over eastern China based on polarimetric radar observations. *J. Geophys. Res. Atmos.* **2016**, *121*, 12415–12433. [[CrossRef](#)]
31. Chen, X.; Zhao, K.; Sun, J.; Zhou, B.; Lee, W.-C. Assimilating surface observations in a four-dimensional variational Doppler radar data assimilation system to improve the analysis and forecast of a squall line case. *Adv. Atmos. Sci.* **2016**, *33*, 1106–1119. [[CrossRef](#)]
32. Doyle, J.D. The Influence of Mesoscale Orography on a Coastal Jet and Rainband. *Mon. Weather Rev.* **1997**, *125*, 1465–1488. [[CrossRef](#)]
33. Fu, S.; Zhang, Y.; Wang, H.; Tang, H.; Li, W.; Sun, J. On the Evolution of a Long-Lived Mesoscale Convective Vortex that Acted as a Crucial Condition for the Extremely Strong Hourly Precipitation in Zhengzhou. *J. Geophys. Res. Atmos.* **2022**, *127*, e2021JD036233. [[CrossRef](#)]
34. Xu, W. Thunderstorm Climatologies and Their Relationships to Total and Extreme Precipitation in China. *J. Geophys. Res. Atmos.* **2020**, *125*, e2020JD033152. [[CrossRef](#)]
35. Zipser, E.J.; Lutz, K.R. Vertical Profile of Radar Reflectivity of Convective Cells: A Strong Indicator of Storm Intensity and Lightning Probability? *Mon. Weather Rev.* **1994**, *122*, 1751–1759. [[CrossRef](#)]
36. Ferrier, B.S.; Simpson, J.; Tao, W.-K. Factors Responsible for Precipitation Efficiencies in Midlatitude and Tropical Squall Simulations. *Mon. Weather Rev.* **1996**, *124*, 2100–2125. [[CrossRef](#)]
37. Market, P.; Allen, S.; Scofield, R.; Kuligowski, R.; Gruber, A. Precipitation Efficiency of Warm-Season Midwestern Mesoscale Convective Systems. *Weather Forecast.* **2003**, *18*, 1273–1285. [[CrossRef](#)]
38. Parker, M.D.; Johnson, R.H. Simulated Convective Lines with Leading Precipitation. Part II: Evolution and Maintenance. *J. Atmos. Sci.* **2004**, *61*, 1656–1673. [[CrossRef](#)]
39. Doviak, R.J.; Zrnić, D.S. *Doppler Radar and Weather Observations*; Academic Press: Cambridge, MA, USA, 1993.

40. Kumjian, M. Principles and applications of dual-polarization weather radar. Part I: Description of the polarimetric radar variables. *J. Oper. Meteorol.* **2013**, *1*, 226–242. [[CrossRef](#)]
41. Kumjian, M.R.; Khain, A.P.; Benmoshe, N.; Ilotoviz, E.; Ryzhkov, A.V.; Phillips, V.T.J. The Anatomy and Physics of ZDR Columns: Investigating a Polarimetric Radar Signature with a Spectral Bin Microphysical Model. *J. Appl. Meteorol. Clim.* **2014**, *53*, 1820–1843. [[CrossRef](#)]
42. Snyder, J.C.; Ryzhkov, A.V.; Kumjian, M.R.; Khain, A.P.; Picca, J. A ZDR Column Detection Algorithm to Examine Convective Storm Updrafts. *Weather Forecast.* **2015**, *30*, 1819–1844. [[CrossRef](#)]
43. Kumjian, M.R.; Lombardo, K.A. Insights into the Evolving Microphysical and Kinematic Structure of Northeastern U.S. Winter Storms from Dual-Polarization Doppler Radar. *Mon. Weather Rev.* **2017**, *145*, 1033–1061. [[CrossRef](#)]
44. Kumjian, M.R.; Prat, O.P. The Impact of Raindrop Collisional Processes on the Polarimetric Radar Variables. *J. Atmos. Sci.* **2014**, *71*, 3052–3067. [[CrossRef](#)]
45. Wang, M.; Zhao, K.; Lee, W.-C.; Zhang, F. Microphysical and Kinematic Structure of Convective-Scale Elements in the Inner Rainband of Typhoon Matmo (2014) after Landfall. *J. Geophys. Res. Atmos.* **2018**, *123*, 6549–6564. [[CrossRef](#)]
46. Carr, N.; Kirstetter, P.E.; Gourley, J.J.; Hong, Y. Polarimetric Signatures of Midlatitude Warm-Rain Precipitation Events. *J. Appl. Meteorol. Clim.* **2017**, *56*, 697–711. [[CrossRef](#)]
47. Ryzhkov, A.V.; Kumjian, M.R.; Ganson, S.M.; Khain, A.P. Polarimetric Radar Characteristics of Melting Hail. Part I: Theoretical Simulations Using Spectral Microphysical Modeling. *J. Appl. Meteorol. Clim.* **2013**, *52*, 2849–2870. [[CrossRef](#)]
48. Zheng, H.; Zhang, Y.; Zhang, L.; Lei, H.; Wu, Z. Precipitation Microphysical Processes in the Inner Rainband of Tropical Cyclone Kajiki (2019) over the South China Sea Revealed by Polarimetric Radar. *Adv. Atmos. Sci.* **2020**, *38*, 65–80. [[CrossRef](#)]
49. Rosenfeld, D.; Ulbrich, C.W. Cloud microphysical properties, processes, and rainfall estimation opportunities. In *Radar and Atmospheric Science: A Collection of Essays in Honor of David Atlas*; Springer: Berlin/Heidelberg, Germany, 2003; pp. 237–258.
50. Dolan, B.; Fuchs, B.; Rutledge, S.A.; Barnes, E.A.; Thompson, E.J. Primary Modes of Global Drop Size Distributions. *J. Atmos. Sci.* **2018**, *75*, 1453–1476. [[CrossRef](#)]
51. Ji, L.; Chen, H.; Li, L.; Chen, B.; Xiao, X.; Chen, M.; Zhang, G. Raindrop Size Distributions and Rain Characteristics Observed by a PARSIVEL Disdrometer in Beijing, Northern China. *Remote Sens.* **2019**, *11*, 1479. [[CrossRef](#)]
52. Wen, L.; Zhao, K.; Chen, G.; Wang, M.; Zhou, B.; Huang, H.; Hu, D.; Lee, W.-C.; Hu, H. Drop Size Distribution Characteristics of Seven Typhoons in China. *J. Geophys. Res. Atmos.* **2018**, *123*, 6529–6548. [[CrossRef](#)]
53. Wen, L.; Zhao, K.; Zhang, G.; Xue, M.; Zhou, B.; Liu, S.; Chen, X. Statistical characteristics of raindrop size distributions observed in East China during the Asian summer monsoon season using 2-D video disdrometer and Micro Rain Radar data. *J. Geophys. Res. Atmos.* **2016**, *121*, 2265–2282. [[CrossRef](#)]
54. Wen, J.; Zhao, K.; Huang, H.; Zhou, B.; Yang, Z.; Chen, G.; Wang, M.; Wen, L.; Dai, H.; Xu, L.; et al. Evolution of microphysical structure of a subtropical squall line observed by a polarimetric radar and a disdrometer during OPACC in Eastern China. *J. Geophys. Res. Atmos.* **2017**, *122*, 8033–8050. [[CrossRef](#)]
55. Miranda, P.M.A.; James, I.N. Non-linear three-dimensional effects on gravity-wave drag: Splitting flow and breaking waves. *Q. J. R. Meteorol. Soc.* **1992**, *118*, 1057–1081. [[CrossRef](#)]

Disclaimer/Publisher’s Note: The statements, opinions and data contained in all publications are solely those of the individual author(s) and contributor(s) and not of MDPI and/or the editor(s). MDPI and/or the editor(s) disclaim responsibility for any injury to people or property resulting from any ideas, methods, instructions or products referred to in the content.